Sub Topic: Fire

SAND2019-10848C

2019 WSSCI Fall Technical Meeting
Organized by the Western States Section of the Combustion Institute
October 14–15, 2019
Albuquerque, New Mexico

Reevaluation of Cellulose Ignition Thresholds Under Extreme Irradiation

Jeffrey D. Engerer[1,*] *and Alexander L. Brown*[1]

[1] *Sandia National Laboratories, 1515 Eubank SE, Albuquerque, NM 87008-1135, USA*
[*] *Corresponding author:* jengere@sandia.gov

Abstract: Ignition of solid materials under convective and/or radiant heating often depends on complex interactions between the solid and fluid phase. Under extreme irradiation ($\gg$100 kW/m^2), historical data suggest the ignition of cellulosic papers is dependent on a simplified set of physics. The initiation and sustainment of ignition is determined from the thickness and thermophysical properties of the solid, and the intensity and duration of radiant heat source. Historical work leverages this reduced parameter set to generate a graphical ignition map, based on two normalized quantities for flux and fluence. We leverage this technique and historical data to produce empirical correlations from the historical data, capturing ignition of cellulose for a range of heating conditions and thermophysical properties. These empirical correlations capture the aleatoric and/or model-form uncertainty with prediction intervals, allowing the user to assess the probability of ignition. We also recommend a small permutation to the historically established normalized variables, collapsing the ignition maps even further. This approach allows simple assessments of ignition modes, transient or sustained, with negligible computational overhead.
Keywords: ***ignition, thresholds, fire, irradiation, cellulose***

1. Introduction

Pyrolysis and ignition of organic materials is commonly studied at incident heat flux ($\approx$10-200 kW/m^2) representative of typical fire environments. A limited range of environments induce heating rates well beyond these limits ($\gg$100 kW/m^2). These environments include metal and propellant fires [1], directed energy [2–4], arc faults [5], and nuclear weapons [6].

Ignition of a solid, especially by flames in the gas-phase, relies on a complex interactions of mechanisms governing the condensed and gas phases. Initially, the solid is inert and the gas-phase is near atmospheric conditions. Energy absorbed by the sample is known and energy transport is well-predicted by Fourier's Law. Upon chemical degradation, the energy-transport physics become increasingly complex, including: enthalpy of pyrolysis, advection of heat & mass, changing surface absorptivity, radiation screening by pyrolysis gases, reradiation, and convective heat loss. The physics of spontaneous ignition increase complexity, requiring successful prediction of localized autoignition amidst large thermal gradients and complex fluid dynamics. Through extensive effort, computational models can account for the myriad physics; however, simplified engineering ignition models are more often preferred, relying on abstracted physics and empirically derived parameters [7].

Martin and his collaborators generated an ignition theory supported by 1000's of tests on carbon-blackened alpha-cellulose papers in the 1950's and 1960's [8–10]. The method was successfully extended to forms of processed cellulose, including: cotton fabric, cardboard, and newspaper [8, 10, 11]. Under this construct, the flux and fluence of the radiant exposure are normalized by the thermophysical properties of the

solid and plotted on a graphical 'ignition map' [12]. Various ignition regimes are defined, and the thresholds between these regimes are repeatable across a range of exposure conditions and sample properties (thickness and density). The utility of the map was limited to high-heat-flux exposures where the effects of convective and radiant losses are negligible.

Adoption of Martin's ignition theory is limited, replaced by theories that better account for physics relevant to typical fire environments. Reviews for ignition at low and moderate heat flux ($\lesssim 100\,\mathrm{kW/m^2}$) criticize the theory as not predictive and ignorant of heat losses (convective and radiative) [7]. The theory is prominently featured in the SFPE handbook [12] and undergirds prominent sources for NW effects [6, 13, 14]. Martin's ignition map is sparsely adopted in recent decades, perhaps due to poor performance at heat flux representative of common fires, and limited interest in ignition at extreme heat flux ($\gg 100\,\mathrm{kW/m^2}$). Recent experimental studies at extreme heat flux have successfully applied the ignition map to cellulosic materials at extreme heat flux, and have had moderate success extending the work to other lignocellulosic and polymeric materials [15].

2. Derivation of the Ignition Map

The historical reports relied predominantly on a graphical approach, producing an 'ignition map.' The ignition map consists of exposure conditions normalized by the thermophysical properties of the solid. The normalized irradiance is defined as:

$$q^* = \frac{a q_o'' L}{k} \tag{1}$$

where q_o'' is the characteristic flux for the exposure (e.g., peak or average), and sample properties a, L, and k are the surface absorptivity, thickness, and thermal conductivity, respectively. The normalized fluence is defined as:

$$Q^* = \frac{a Q''}{\rho c_p L} \tag{2}$$

where Q'' is the exposure fluence, ρ is the density, and c_p is the specific heat. Normalized irradiance, q^*, and normalized fluence, Q^*. Normalized irradiance and normalized fluence each have units of temperature (K). Revealing the theoretical basis in thermal diffusion, the ratio of the normalized fluence and normalized irradiance is the Fourier number:

$$\frac{Q^*}{q^*} = \frac{a Q''/\rho c_p L}{a q_o'' L/k} = \frac{\alpha}{L^2}\frac{Q''}{q_o''} = \frac{\alpha t^*}{L^2} = Fo^* \tag{3}$$

where the characteristic time, t^*, is the ratio of the fluence to the characteristic flux. For a square-wave exposure, t^* is simply the duration of the exposure.

Data were collected for exposures with constant intensity and exposures simulating dynamic thermal irradiation from a nuclear-weapon airburst. The flux and fluence produced by each exposure type are compared in Fig. 1a; each exposure has the same peak flux and total fluence. These exposure shapes are referred to as "SW" for "square wave" and "NW" for "nuclear weapon." The NW exposure ends abruptly at $t = 10t_p$, where t_p is the peak time [16].

Ignition-threshold data produced by Martin et al. for both SW and NW exposures are provided in Fig. 1b [8, 9, 17]; data in this form constitute an ignition map. Unlike the standard method for cone calorimeters [18], Martin and his collaborators did not identify the time of ignition during a uniform, continuous heat load. Instead, experiments varied the exposure duration, and categorically defined the ignition mode produced at the exposure end. Consequently, data points on the ignition map are based on threshold exposures, producing the corresponding ignition mode at the last viable moment.

The threshold exposures were determined by setting the exposure intensity and modulating the exposure duration. Using over 20 experiments per exposure intensity, the experiments characterized the threshold

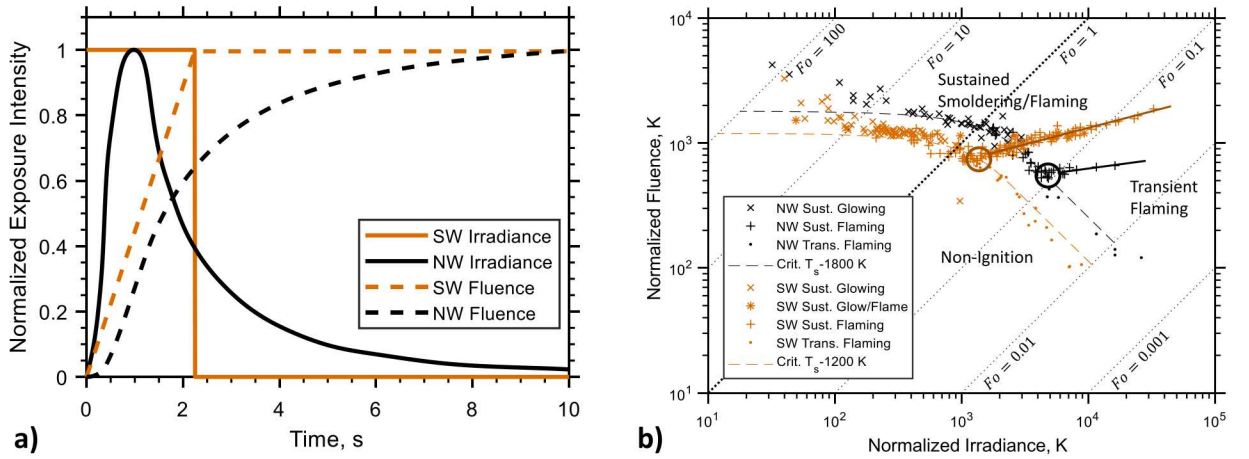

Figure 1: Historical data generated for black α-cellulose papers irradiated by the SW and NW exposures [8–10]. (a) Irradiance (solid) and fluence (dashed) of historical exposure profiles. Each exposure has the same peak irradiance and total fluence. Irradiance and fluence are normalized by their peak values. (b) Ignition maps developed by the historical data. Lower thresholds, upper thresholds, and branch points annotated using dashed lines, solid lines, and circles, respectively. Dotted lines indicate constant Fourier number; the bold dotted line is at $Fo = 1$.

exposure time, including the mean, standard deviation, and standard-error of the mean [9]. A statistical analysis was performed on the exposure-time requirements for square-wave exposures [9]. Exposure time resolution was 1 ms. Standard error of the mean (i.e., confidence interval) typically varied between 0.7-3.4 %. The standard deviation was roughly three times the standard error of the mean and typically ranged between 1.0-10.6 %. The Mitchell heat source had moderate spatial and temporal variability (i.e., aleatory uncertainty), estimated at 5 % [19]. The calorimeter used to evaluate the irradiance produced by the Mitchell heat source had an estimated calibration error (i.e., epistemic uncertainty) of 2.8 % [20].

When applying the map to ignition predictions, the irradiance and fluence of the heat source are normalized (Equations 1 and 2) and compared to the thresholds on the map. The ignition mode is determined by the region where the exposure falls on the ignition map, including: non-ignition, sustained smoldering or flaming, and transient flaming. These regions are bounded by the lower (dashed) and upper (solid) thresholds. Ignition thresholds depend on the dynamic profile of the exposure (e.g., SW and NW exposures). Lower thresholds were estimated using analytical solutions for heat diffusion (later defined in Equation 5) and arbitrary critical surface temperatures (1200 K for SW, 1800 K for NW). The map is formulated based on irradiance and fluence of the entire exposure, and was not demonstrated to predict ignition timing for an exposure exceeding the threshold.

In the lower-left region, normalized irradiance and normalized fluence are relatively low; no ignition is expected, regardless of the Fourier number. In the lower-right region of the map, normalized irradiance is high, but normalized fluence is low. The Fourier number is very low (Fo$\ll$1), indicating that heating is limited to a thin surface layer. For α-cellulose, these conditions resulted in a hot surface that emanated flames, but because the bulk material remained relatively cool, the surface temperature rapidly dropped and flaming ceased when the exposure ended. This ignition mode was identified as transient flaming.

The upper-left region of the map indicates high normalized fluence and low normalized irradiance. The Fourier number is relatively large (Fo$\gg$1); consequently, the bulk material is heated significantly and thermal gradients are minimized. Ignition in this region is predominantly by sustained smoldering (i.e., sustained glowing). Smoldering typically continued until the sample was consumed.

In the upper-right region of the map, the exposures feature high normalized fluence and moderate-to-high normalized irradiance. The Fourier number is typically near unity, indicating moderate thermal

gradients within the solid. The α-cellulose papers tended to exhibit sustained flaming ignition in this region. The normalized fluence required for sustained ignition is reduced near the branch point, especially for NW exposures.

The point at which the sustained-, transient-, and non-ignition modes meet is the branch point (circles in Fig. 1b). The lower threshold bounds cases of non-ignition and ignition (of any type). The upper threshold bounds cases of transient and sustained ignition. The thresholds and branch points in Fig. 1b are denoted notionally.

Based on a more limited data set, the ignition map well-predicted ignition modes for other nearly pure cellulose materials, namely: newspaper, cardboard, and cotton fabric [8, 10]. The utility of the ignition map for other materials was not demonstrated.

As indicated by the existence of two sustained ignition types, the sustained ignition regime is divided into two corresponding regions, sustained smoldering and sustained flaming. Although this threshold was examined in some of the historical literature [16], the transition was generally not the focus of these reports. The transition between these sustained modes is poorly captured by the normalized variables and is dependent on apparatus and scale [16]. Thus the ignition map leverages a convenient coincidence of the lower-sustained ignition limit, bypassing the complex requirements of a gas-phase ignition model.

Martin also used the map to define three regimes that were controlled by convection, thermal diffusion, or ablation. The diffusion-controlled regime is the focus of the map. In the convection-controlled regime, normalized fluence diverges from the plateau as normalized irradiance decreases, eventually reaching an asymptote [21]. In the ablation-controlled regime, surface recession exceeds the rate of thermal diffusion, indicated by low Fourier number. At very high heat flux (up to $4\,\mathrm{MW/m^2}$) exposures just below the upper threshold left behind a very thin layer of material ($\approx 50\,\mu\mathrm{m}$) regardless of the original sample thickness [10]. Although not strictly defined, bounding values of normalized irradiance were proposed in prior work [21]. For $q^* < 400\,\mathrm{K}$, ignition was considered convection controlled. For $400\,\mathrm{K} < q^* < 10\,000\,\mathrm{K}$, ignition was diffusion controlled. For $q^* > 10\,000\,\mathrm{K}$, ignition was ablation controlled.

When comparing ignition thresholds for SW and NW exposures, there is a notable offset between the corresponding ignition thresholds. The apparent requirements for surface heating are roughly 60% higher for the NW exposures Alternatively, Martin suggested multiplying the peak irradiance by a factor of 0.37 [9]. Even with this empirical correction factor, the normalized-irradiance threshold is still mismatched: up to 30 % more irradiance is required for sustained ignition at low flux and 30-40 % less energy is required at the upper threshold. No method for equating to SW exposures thresholds was determined [9].

While the threshold ignition events (e.g., exposures defining the boundaries between ignition regimes) always ignited at the end of square-wave exposures, the ignition time varied for NW exposures. For short-duration, high-intensity exposures, ignition occurred "well out on the tail of the pulse; some time after the peak" [16]. Meanwhile, for long-duration, low-intensity exposures, ignition occurred shortly after the peak, and "appears to approach the peak time as a limit" [16]. The actual ignition time was unrecorded in the historical NW-exposure data [9].

3. Empirical Correlation for SW Exposures

Empirical correlations are derived for the lower- and upper-ignition thresholds, using prediction intervals to capture the spread in the data. Using the Fourier number as the dependent variable, our objective is to determine the normalized fluence for threshold exposures, Q^*_{th}, using the historical SW-exposure data [8]. The non-linearity of the lower threshold is captured using an analytical heat-transfer solution and an empirically derived fitting parameter, the critical surface temperature rise. The upper-threshold is captured in a similar manner, but without reliance on the analytical solution.

The lower threshold is derived from the surface temperature of a inert solid radiantly heated by a constant load [22]:

$$\frac{k\left[T_{(x=0,Fo)}-T_i\right]}{aq_o''L}=Fo+\frac{2}{\pi^2}\sum_{m=1}^{\infty}\frac{1}{m^2}\left(1-e^{-m^2\pi^2Fo}\right) \tag{4}$$

where m is the index of summation. The critical surface temperature rise, ΔT_{th}, defines the threshold values for the Fourier number, Fo_{th}, and normalized irradiance, q^*_{th}. Applying the relation for the normalized irradiance (Equation 1), the threshold conditions are:

$$\frac{\Delta T_{th}}{q^*_{th}}=Fo_{th}+\frac{2}{\pi^2}\sum_{m=1}^{\infty}\frac{1}{m^2}\left(1-e^{-m^2\pi^2Fo_{th}}\right) \tag{5}$$

Recognizing the normalized fluence is the product of the normalized irradiance and the Fourier number (Equation 3), the following expression predicts the threshold normalized fluence:

$$Q^*_{th}=q^*_{th}Fo_{th}=\Delta T_{th}f(Fo_{th}) \tag{6}$$

where $f(Fo)$ is the fraction:

$$f(Fo)=\frac{Fo}{Fo+\frac{2}{\pi^2}\sum_{m=1}^{\infty}\frac{1}{m^2}\left(1-e^{-m^2\pi^2Fo}\right)} \tag{7}$$

Equation 6 is the basis for the experimental correlation; however, because the data span many orders of magnitude, a logarithmic transform (base-10) is advantageous:

$$\log Q^*_{th}=\log\Delta T_{th}+\log f(Fo_{th}) \tag{8}$$

The critical surface temperature rise is calculated from the historical square wave data for the lower threshold [8] using Equation 8 and plotted in Fig. 2a. The convection-controlled regime is neglected by eliminating data with very high Fourier number ($Fo>15$). The critical surface temperature varies with Fourier number from 1000 K ($Fo\approx 0.01$) to 1400 K ($Fo\approx 10$). The following empirical correlation captures this linear trend:

$$\log\Delta T_{th}=A_0+A_1\log Fo_{th} \tag{9}$$

where A_0 is $3.09\pm0.16\%$ and A_1 is $0.0523\pm14.3\%$ (90% confidence). The root mean square error is 0.0318, and the predicted R-squared[1] is 0.517. Returning to Equation 8, the following correlation determines the threshold normalized fluence:

$$\log Q^*_{th}=A_0+A_1\log Fo_{th}+\log f(Fo_{th}) \tag{10}$$

The sustained-flaming ignition thresholds are relatively scattered compared to other ignition modes. Many sustained-flaming cases exhibit significant suppression ($\approx 20\%$) in the critical surface temperature rise. No predictive correlation (high predicted R-squared) was found for this variation.

An empirical correlation can likewise be employed to quantify the upper ignition threshold. Unlike the highly non-linear behavior of the lower threshold, the upper threshold is captured by a simple correlation, without invoking transient-heat-transfer calculations, and has the following form:

$$\log Q^*_{th}=B_0+B_1\log Fo_{th} \tag{11}$$

where B_0 is $2.84\pm1.1\%$, B_1 is $-0.286\pm20\%$. The root mean square error is 0.0376.

[1] Predicted R-squared evaluates correlations for predictiveness, and should not be confused with the R-squared value, which evaluates goodness-of-fit.

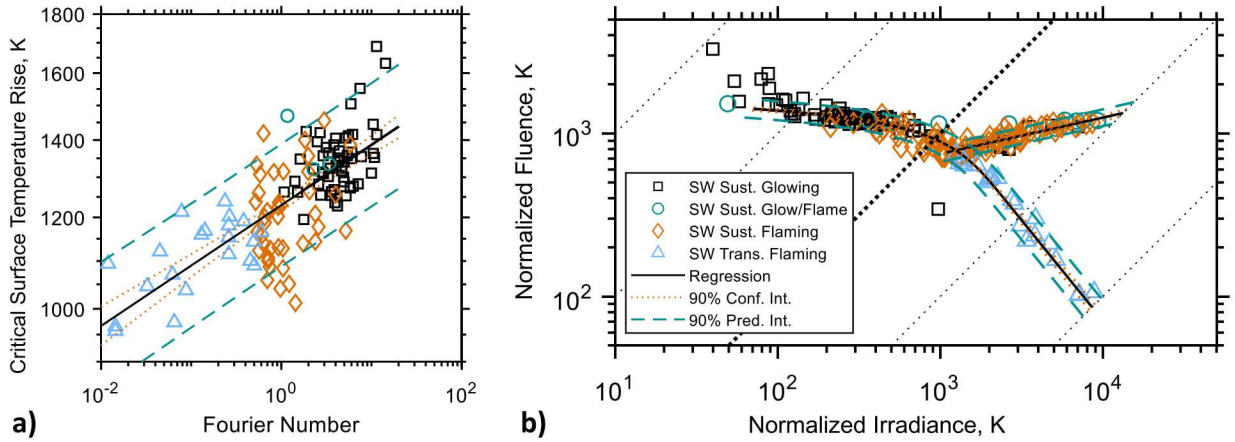

Figure 2: Deriving the upper- and lower-threshold correlations for SW exposures [8]. (a) Determination of the critical surface temperature rise for the lower threshold of SW exposures [8]. (b) Correlations compared to historical ignition map. Dotted lines indicate constant Fourier number; the bold dotted line is at $Fo = 1$.

The correlations for the upper- and lower-thresholds can be rewritten to predict normalized irradiance, using Equation 3. For many applications, the inverse problem is more logical (Fo_{th} as a function of q^*_{th}), and can be easily solved (e.g., by tabulation).

Using Equation 10 and Equation 11, the lower and upper ignition thresholds are well-characterized, as demonstrated by Fig. 2b. The upper-threshold correlation (Equation 11) sufficiently resolves the cutoff from transient to sustained ignition along the lower threshold. Both thresholds should be exceeded for sustained-ignition events. If only the lower threshold is exceeded, transient-flaming ignition is predicted.

4. Reducing the Effect of Exposure Shape

In many practical applications, the radiant exposure varies dynamically, such as the NW exposure provided in Fig. 1a. Using the formulation presented in prior reports, the effect of exposure shape cannot be derived, and a different ignition map must be formulated for each potential exposure shape (Fig. 1b) [8, 9].

The SW and NW exposures have two important differences that are poorly captured when basing ignition maps on peak irradiance and total fluence. First, the peak irradiance during an NW exposure is maintained only for a very brief time. Consequently, comparing the peak irradiance directly to a SW exposure is likely to underestimate the likelihood of ignition. Second, much of the energy contained by the exposure is transmitted by the long, low-intensity tail (Fig. 1a). At the peak, only approximately 27% of the total fluence has been delivered. 25% of the total fluence is provided by the tail beyond $t = 3t_p$, even though the irradiance has fallen by $\approx$75%. Depending on when ignition occurs in relation to the peak, much of the exposure fluence may be delivered after the onset of ignition.

Consequently, the NW thresholds are expected at higher normalized irradiance and normalized fluence than SW thresholds, provided peak irradiance and total fluence define the respective normalized variables. This trend is clearly exhibited in the ignition map (Fig. 1b). To align the NW-exposure data to the SW data, an empirically derived 'shape factor' could be applied to the normalized quantities in the ignition map [9]. Alternatively, a new critical surface temperature rise could be defined, as in Section 3. However, these approaches require parameters that are empirically derived, requiring extensive experimentation. An approach that leverages the expansive data set for SW exposures is preferred.

We reduced the impact of exposure shape on the lower threshold by implementing two modifications

to the normalized threshold quantities. The first modification uses the normalized fluence and the Fourier number (replacing normalized irradiance). The second modification evaluates these variables upon ignition, namely: the time and net fluence at ignition. When implementing these changes, the normalized irradiance is effectively based on the temporally averaged irradiance, up to the time of ignition.

For SW exposures, these modifications do not change the ignition map, because ignition is presumed to occur at the end of the exposure. Consequently, the modified form still evaluates the total fluence and the peak irradiance (which is the same as the average).

However, the threshold variables for dynamic exposure profiles do change. Unfortunately, only qualitative information was provided for the time-of-ignition during NW exposures. Reports indicate the time of ignition is well after the peak for high-intensity, low-duration exposures, and approaches the peak as exposures become progressively longer and less intense [16].

Ignition cannot occur once irradiance falls below certain values. During a threshold exposure, ignition occurs at the latest viable time in the exposure. Leveraging these two assumptions, we estimate the ignition time by defining the minimum irradiance required for flaming and smoldering ignition. As will be explained later, both minimum irradiances require only an order-of-magnitude estimate.

For flaming ignition, the minimum irradiance is governed by either (a) sufficient heating of the pyrolyzate or (b) production of pyrolyzate in sufficient quantities. Conveniently, the minimum irradiance is reasonably well-characterized by the SW exposures on the same apparatus. Leveraging this expansive data set, the minimum irradiance is determined by the exposure irradiance below which flaming ignitions no longer occur and is roughly $100\,\mathrm{kW\,m^{-2}}$.

For smoldering ignition, the minimum irradiance is governed by the solid-phase temperature. We adopt the smoldering surface temperature proposed by Martin, 450 °C [17]. By assuming smoldering ignition initiates when the surface reaches this temperature, we conclude a threshold exposure reaches 450 °C at the last viable moment, just as heat loss overtakes incident heat flux. Recognizing that radiant heat loss dominates at high temperatures, the minimum irradiance for smoldering ignition is approximated as $15\,\mathrm{kW/m^2}$ using the Stefan-Boltzmann Law.

The time-of-ignition threshold data for NW exposures, defined by these minimum irradiance values ($100\,\mathrm{kW\,m^{-2}}$ for flaming, $15\,\mathrm{kW\,m^{-2}}$ for glowing), are compared to the SW data in Fig. 3. This modified form of the ignition map (*Fo* and Q^*_{th} at ignition) improves agreement for the lower threshold in two significant ways. First, time-of-ignition data collapses the threshold data for NW-exposures onto those for SW-exposures. Second, the modified ignition map reduces the spread in the NW-exposure data. The dependence of the upper thresholds on exposure type is not captured by modified ignition map.

The minimum irradiance for smoldering and flaming ignitions are clearly only estimates. Fortunately, the data are insensitive to the exact magnitude of the minimum irradiance values. Both minimum irradiance criteria were increased and decreased by a factor of two, and only a few data points for flaming-ignition thresholds changed significantly. In fact, better agreement was obtained when the minimum irradiance for smoldering ignition was twofold higher. The insensitivity arises from (1) the shape of the NW exposure and (2) the location of smoldering ignition thresholds on the ignition map.

Flaming ignition requires higher irradiance, and typically occurs shortly after the peak. The steep drop-off in irradiance renders time-of-ignition insensitive to the minimum irradiance for flaming. Smoldering ignition requires less irradiance, and can occur well into the NW-exposure tail. Although the extended tail causes the time-of-ignition to be very sensitive to the minimum irradiance for smoldering, these smoldering ignition events typically occur in a region of the map dominated by normalized fluence. Exposure fluence reaches a plateau in the tail and, consequently, remains insensitive to the minimum irradiance.

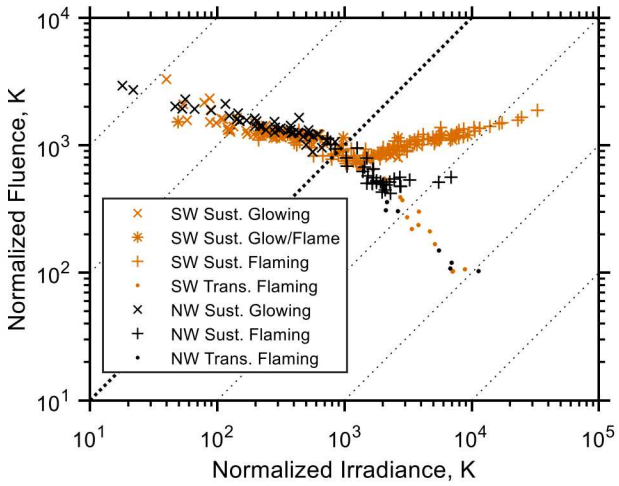

Figure 3: Proposed, modified form for the ignition map using historical data of Martin et al. [8–10]. Threshold data for SW and NW exposures are compared using the Fourier number and normalized fluence at the time of ignition. Dotted lines indicate constant Fourier number; the bold dotted line is at Fo=1.

5. Discussion

The requirement to determine the time-of-ignition in threshold exposures only appears necessary when the dynamic profile includes a long, extended tail, such as the NW exposure used by the historical reports. If the exposure ends abruptly, the fraction of the total fluence delivered near the end, below the minimum irradiance is negligible. Therefore, the fluence and time of the entire exposure likely remains valid, as it is for SW exposures. In other words, the only recommended change for dynamic exposures that end abruptly is to use the average irradiance of the profile. This approach successfully predicted ignition produced by dynamic exposures for a variety of cellulose papers [15].

If the exposure includes a long extended tail, the method for estimating the time-of-ignition used in Section 4 is not preferred. The time of ignition is better determined by instrumentation, such as visible or infrared imagery. Flame detection was successfully deployed in recent high-heat-flux experiments [15] using visible-light cameras; however, initiation of smoldering ignition during the high intensity exposure was not observable. Further studies are recommended to validate these approaches for a variety of exposures profiles, with and without extended tails.

The dominant physics of the upper threshold remain unresolved. NW exposures require roughly half the normalized fluence to sustain ignition (Fig. 1b). Moreover, the use of minimum irradiance to determine the exposure quantities at the time of ignition (Fig. 3) is arbitrary, since these exposures typically ignite by transient ignition before reaching the sustained ignition limit. An alternate version of the map using total exposure fluence and time for the upper threshold yielded unfavorable results (increase in data scatter, collapsing of data points below the lower threshold). These physics governing the upper threshold require further study. Our recommendation is to develop a second engineering model for this limit, focusing on the temperature gradient at the surface at the end of the exposure.

The historical ignition maps are exclusively based on threshold exposures. This approach meets the objectives of relevant applications, differentiating between exposures that cause ignitions and those that do not. However, when formulating the ignition maps, resolving threshold exposures is labor-intensive, requiring many experiments, such as the staircase method used in the historical reports [8–10]. A more efficient approach is to use the time-of-ignition data to determine ignition requirements.

The modifications to the ignition map developed in the Section 4 may allow comparisons to time-of-

ignition data. The validity of this this method is plausible, given that the threshold data for NW exposures better collapse to SW-exposure data when the time, flux, and fluence beyond ignition are neglected. This approach was successfully applied to the flaming-ignition of cellulosic papers exposed to dynamic irradiance profiles [15]. A dedicated study to confirm the validity of this approach is recommended. If successful, this technique would substantially reduce the number of experiments required to determine the lower-threshold for flaming-ignition events.

Over-reliance on flame detection could compromise the data. In small-scale apparatuses, smoldering- and flaming-ignition thresholds diverge at high Fourier number. If the objective is to determine the lower threshold (i.e., replicate the ignition map), flame detection in exposures exceeding the threshold could provide erroneous estimates. We recommend performing experiments below the threshold determined by the time-of-ignition method, to determine if/when the flaming ignition threshold diverges from the lower threshold. This approach successfully captured cases of divergent thresholds for a variety of materials [15].

The reported values for the critical surface temperature rise (1000-1400 K) are well above the physical surface temperatures (600 °C or less) reported experimentally [23]. The temperature overprediction indicates that roughly half of the exposure irradiation is absorbed or rejected by other physical mechanisms. Many mechanisms could account for this over prediction, including: radiation screening by pyrolysis gases, convective losses, reradiation, and ignition delays. However, none of these mechanisms simultaneously explain the large discrepancy and the strong correlation with the Fourier number (e.g., dependence on thickness).

The enthalpy of pyrolysis is a plausible explanation. The heat of pyrolysis could absorb thermal energy in a manner analogous to the specific heat of the material, namely: the resulting thermal sink is localized to the heated region in the solid. Scaling with the Fourier number is expected, to first order.

Given the basis of the ignition map in thermal diffusion, application of the map is likely only valid if ignition is dominated by heating of the solid phase. Any significant ignition delay or thermal effect arising from gas-phase phenomena is unlikely to be strongly coupled to the thermal state of the solid.

The ignition maps for SW and NW exposures were formulated under a limited set of conditions. The maps are based on black α-cellulose samples, with a limited range of thicknesses and exposure conditions. Limited experiments were performed on other processed-cellulose samples (cotton fabric, cardboard, and newspaper). Consequently, the utility of the map must be demonstrated before extending beyond this scope. A variety of material parameters are likely to influence the ignition map, especially those that affect the integrity of the critical-surface-temperature-rise estimation. For example, recent data on white cellulose papers [2] have revealed unexpected ignition modes, perhaps due to low surface absorptivity and/or diathermicity [15].

Extension of the ignition map to field environments at larger scale introduces complexities that may impact the underlying physics. Prior studies suggest the lower threshold for cellulose remain unchanged at larger scale, but flaming-ignition modes become more common [16, 24]. Exposures just below the upper threshold are characterized by transient flames that extinguish when the heat source is removed. At larger scale, heating of the surface from the flame sheath is increased, and may be augmented by irradiation from other hot surfaces and combustion events in the surrounding area. If these effects significantly impact the surface energy balance ($\gg 10\,\mathrm{kW/m^2}$), the upper threshold could be lowered substantially. The reduction in the upper threshold due to the extended tail of the NW exposures is perhaps evidence of these effects. An engineering ignition model better suited to the upper threshold may resolve these physics.

The trends and physics revealed by the ignition map suggest models based on total exposure fluence [6] are deficient for cellulose. Fluence-based models neglect the possibility of transient ignition. For sustained ignition by NW exposures, the threshold fluence at small scale varies by a factor of four. As was discussed above, increased heat feedback to the surface at larger scale could increase this disparity.

The ignition map has a strong experimental basis (1000's of experiments) but is very narrow in scope,

[2] Statement is based on cited document, and updated (lower) surface absorptivity values from reflectance measurements.

namely: darkened fabrics and papers made from processed cellulose. A much wider range of materials are relevant to extreme-heat-flux ignition. Extension of the general theory to white cellulose products, lignocellulosics (e.g., plant matter, wood), fabrics (e.g., wool, rayon, synthetic polymers), and thin films (e.g., polyethylene and other plastics) could better reconcile ignition models at extreme heat flux. The locations of the thresholds are likely to change for each material, but the general approach may remain valid for a broader range of materials. Recent experimental studies have had some success with this approach [15, 25].

6. Conclusions

The ignition map developed by Martin and his collaborators has been revised to include empirical correlations, uncertainty analysis, the effects of exposure shape, and time-of-ignition data. Although the map is infrequently adopted for normal fire environments, the results improve capabilities for ignition assessments at extreme heat flux ($\gg 100\,\mathrm{kW/m^2}$). Results for the lower threshold are promising, but engineering models for the upper threshold remain unresolved. Future studies are recommended to validate these approaches on other data sets.

Acknowledgments

We appreciate programmatic support from Jon Rogers (SNL). Funding was provided by the Defense Threat Reduction Agency. Sandia National Laboratories is a multimission laboratory managed and operated by National Technology and Engineering Solutions of Sandia, LLC, a wholly owned subsidiary of Honeywell International, Inc., for the U.S. Department of Energy's National Nuclear Security Administration under contract DE-NA0003525. This paper describes objective technical results and analysis. Any subjective views or opinions that might be expressed in the paper do not necessarily represent the views of the U.S. Department of Energy or the United States Government.

References

[1] R. B. White, S. W. Dean, M. L. Pantoya, D. A. Hirschfeld, W. Gill, and W. W. Erikson, Effect of Aluminum on Heat Flux from a Simulated Rocket Propellant Flame, Journal of Propulsion and Power 23 (2007) 1255–1262. DOI: 10.2514/1.28161.

[2] N. Mutoh, T. Hirano, and K. Akita, Experimental study on radiative ignition of polymethylmethacrylate, 17th Symp. (Intl.) on Combustion The Combustion Institute, (1978), pp. 1183–1190.

[3] T. Kashiwagi, Experimental Observation of Radiative Ignition Mechanism, Combustion and Flame 34 (1979) 231–244.

[4] J. Geiss, Directed energy weapons on the battlefield: A new vision for 2025, Report Report No., Air University, 2003.

[5] Y. Cressault, A. Gleizes, and G. Riquel, Properties of air–aluminum thermal plasmas, Journal of Physics D: Applied Physics 45 (2012), DOI: 10.1088/0022-3727/45/26/265202.

[6] S. Glasstone and P. Dolan, The Effects of Nuclear Weapons, 3rd ed., U.S. Department of Defense and U.S. Department of Energy, 1977.

[7] V. Babrauskas, "Common Solids", in: Ignition Handbook, Fire Science Publishers, Issaquah, WA, 2003, chap. 7, pp. 234–351.

[8] C. P. Butler, S. B. Martin, and W. Lai, Thermal radiation damage to cellulosic materials: Part II. Ignition of alpha cellulose by square-wave exposure, Report Report No., US Naval Radiological Defense Laboratories, 1956.

[9] S. B. Martin and W. Lai, Thermal radiation damage to cellulosic materials: Part III. Ignition of alpha cellulose by pulses simulating nuclear weapon air blasts, Report Report No., US Naval Radiological Defense Laboratories, 1958.

[10] S. B. Martin, Ignition of cellulosic kindling fuels by very brief radiant pulses, Report Report No., U.S. Naval Radiological Defense Laboratory, 1963.

[11] S. B. Martin, Ignition of organic materials by radiation, Fire Research Abstracts and Reviews 6 (1966) 85–98.

[12] A. M. Kanury, Flaming ignition of solid fuels, 3rd ed., SFPE Handbook of Fire Protection Engineering, Society of Fire Protection Engineers, Quincy, MS, 2002, pp. 2-229–2-245.

[13] A. M. Kanury, SFPE classic paper review: Diffusion-controlled ignition of cellulosic materials by intense radiant energy by Stanley B. Martin, Journal of Fire Protection Engineering 19 (2009) 125–131. DOI: 10.1177/1042391508101990.

[14] W. Strope and J. Christian, Fire aspects of civil defense, Fire Research Abstracts and Reviews 7 (1965) 155–166.
[15] J. D. Engerer, A. Brown, and J. Christian, Ignition and Damage Thresholds of Materials at Extreme Incident Radiative Heat Flux, 2018 Joint Thermophysics and Heat Transfer Conference AIAA, (2018), p. 3764.
[16] S. B. Martin and N. J. Alvares, Ignition thresholds for large-yield nuclear weapons, Report Report No., US Naval Radiological Defense Laboratory, 1966.
[17] S. B. Martin, Fire setting by nuclear explosion: A revisit and use in nonnuclear applications, Journal of Fire Protection Engineering 14 (2004) 283–297. DOI: 10.1177/1042391504044541.
[18] ASTM, *Heat and visible smoke release rates for materials and products using an oxygen consumption calorimeter*, Standard, 2017, DOI: 10.1520/e1354-17.
[19] T. R. Broida, The production of intense beams of thermal radiation by means of high current carbon arc and relay-condenser optical system, Report Report No. USNRDL-417, U.S. Naval Radiological Defense Laboratory, 1953.
[20] A. Broida and A. B. Willoughby, Measurement of intense beams of thermal radiation, Journal of the Optical Society of America 48 (1958) 344–350.
[21] S. B. Martin, Diffusion-controlled ignition of cellulosic materials by intense radiant energy, Tenth Symposium (International) on Combustion (1965), pp. 877–896.
[22] K. Cole, J. V. Beck, A. Haji-Sheikh, and L. Bahman, Heat Conduction Using Green's Functions, Taylor & Francis, 2011.
[23] N. J. Alvares, Measurement of the temperature of the thermally irradiated surface of alpha cellulose, Report Report No., US Naval Radiological Defense Laboratories, 1964.
[24] A. L. Brown, J. D. Engerer, A. Ricks, and J. Christian, Scale Dependence of Material Response at Extreme Incident Radiative Heat Flux, 2018 Joint Thermophysics and Heat Transfer Conference AIAA, (2018), p. 3762, DOI: 10.2514/6.2018-3762.
[25] A. Brown, J. D. Engerer, A. Ricks, and J. Christian, Initiation of pyrolysis from high flux exposures, 2019 WSSCI Fall Technical Meeting Western States Section of the Combustion Institute, (2019).